Available online at www.sciencedirect.com

ScienceDirect

Advances in Space Research 62 (2018) 809–820

ADVANCES IN SPACE RESEARCH (a COSPAR publication)

www.elsevier.com/locate/asr

3-D ionospheric tomography from dense GNSS observations based on an improved two-step iterative algorithm

Shuanggen Jin [a,b,*], Du Li [c]

[a] School of Remote Sensing and Geomatics Engineering, Nanjing University of Information Science and Technology, Nanjing 210044, China
[b] Shanghai Astronomical Observatory, Chinese Academy of Science, Shanghai 200030, China
[c] School of Communication and Information Engineering, Shanghai University, Shanghai 200444, China

Received 15 December 2017; received in revised form 19 May 2018; accepted 21 May 2018
Available online 1 June 2018

Abstract

Computerized ionospheric tomography (CIT) can image 3-D ionospheric variations from ground Global Navigation Satellite System (GNSS) observations. However, due to the sparse and inhomogeneous ground GNSS observations, the prior information from the empirical models (e.g., IRI-2012 and NeQuick 2) have to be used, which affect the reconstructed results in the CIT, particularly the peak parameters of the F2 layer, namely *foF2* and *M(3000)F2*. In this paper, an improved two-step CIT algorithm is developed to image the ionospheric electron density (IED) distribution up to 2000 km over Japan using dense GNSS Earth Observation Network (GEONET) observations operated by the Geospatial Information Authority (GSI) of Japan. Firstly, we update the IRI-2012 using the ground-based GNSS observations. The NeQuick-2 is used to provide the vertical ionospheric profile, and *foF2* and *M(3000)F2* derived from CCIR model in NeQuick 2 are improved by the B-spline modeling methods. Secondly, the updated IRI-2012 is input as a prior value and the multiplicative algebraic reconstruction technique (MART) is implemented to reconstruct the IED distribution. The reconstructed results are validated by the simulation and observation results from ground-based GNSS, GNSS Radio Occultation (GNSS-RO) observations and ionosonde measurements. The results demonstrate the feasibility and superiority of our new method. The standard deviations of TEC residual errors from the updated NeQuick 2 are at least 20% less than those from the original NeQuick 2 model, and the updated NeQuick 2 has better performance for the ionospheric correction.

Keywords: Ionospheric electron density (IED); GNSS; NeQuick 2; MART

1. Introduction

Ionospheric monitoring plays an important role in the studies of space weather and ionospheric delay correction, particularly in the navigation and trans-ionospheric communication fields, such as the satellite positioning and navigation. The effect of the ionosphere on the specific signal waves, called the ionospheric delay, is mainly attributable to the ionospheric electron density or its integration along the signal path, namely the total electron content (TEC) (Jin et al. 2004, 2007, 2013). The single layer ionospheric model is one of the most widely used models, where the electron content is concentrated on a thin layer at a given height (Montenbruck et al., 2014). However, the single layer model only reflects the variation of the ionosphere in the horizontal plane but neglects the variation along the altitude. Computerized ionospheric tomography (CIT) is a technique to reconstruct the 2-D, 3-D or 4-D ionospheric images (Bust and Mitchell, 2008; Razin, 2016). Since Austen et al. (1986) firstly introduced the computerized tomography (CT) to reconstruct 2-D ionospheric

* Corresponding author. Tel.: +86 25 58235371.
E-mail addresses: sgjin@nuist.edu.cn, sgjin@shao.ac.cn (S. Jin).

https://doi.org/10.1016/j.asr.2018.05.032
0273-1177/

images, a number of significant works on ionospheric tomography were reported based on the CIT technology (Jin and Park, 2007; Bust and Mitchell, 2008; Jin et al., 2008; Seemala et al., 2014). Nowadays, Global Navigation Satellite Systems (GNSS), including GPS, BeiDou, Galileo and GLONASS (Jin and Park, 2006; Najibi and Jin, 2013), provide precise TEC measurements to image ionospheric information with increasing large number of worldwide distributed GNSS observations (Jin et al., 2011).

Since CIT is essentially an ill-posed problem due to the sparse and uneven distribution of ground-based GNSS observations, a number of methods were proposed to solve the ill-conditioned problem, including the iterative algorithms (Jin et al., 2006; Yao et al., 2015; Wen et al., 2007; Kunitsyn et al., 2011), the non-iterative algorithms (Kunitake et al., 1995; Bhuyan et al., 2004) and the data assimilation techniques (Yue et al., 2012; Aa et al., 2016). Most effective solutions are realized by the employment of the ionospheric background models or the constraints, such as IRI-2012 and NeQuick. The chosen empirical ionospheric models as the background can be used as initial values for the CIT solutions, and therefore a high precision background model is an effective approach to improve the reconstructed results in the CIT. For empirical ionospheric models, especially the three commonly used IRI, NeQuick and simple α-chapman models, the critical frequency *foF2* and the propagation factor *M(3000)F2* of the F2 layer, are the two main driving parameters in the description of the vertical ionospheric profile.

The NeQuick model was developed based on the modified DGR (Di Giovanni and S.M. Radicella) model at the Aeronomy and Radiopropagation Laboratory of the Abdus Salam International Centre for Theoretical Physics (ICTP), Italy and at the Institute for Geophysics, Astrophysics, and Meteorology of the University of Graz, Austria. Continuous improvements have been made to the NeQuick model. The latest version is NeQuick 2, which keeps the conceptual structure but modifies the formulation of some parameters in contrast to the first version. The NeQuick model gives the ionospheric electron density anywhere and anytime, and also provides TEC along any satellite-to-ground signal path (Yu et al. 2015; Nava et al. 2008). It has been widely used in the trans-ionospheric radio propagation field for the high precision and high computational efficiency in obtaining TEC. The NeQuick model has been adopted by the International Telecommunication Union, Radiocommunication Sector (ITU-R) to model the TEC. In addition, the first version of the NeQuick model served for system assessment analysis in the European Geostationary Navigation Overlay Service (EGNOS) project operated by the European Space Agency (ESA), such as the simulation for the disturbed ionospheric scenarios. It has been used to implement ionospheric corrections for single-frequency positioning of the European GALILEO system (Angrisano et al., 2013). Three profile anchor points, namely the E-peak point, the F1 peak point and the F2-peak point are used to describe the vertical ionospheric profile.

The IRI model can predict 3-D monthly averages of the ionospheric electron density, which often overestimates or underestimates the IED values (Jin and Park, 2007). The F2-peak parameters used in the IRI model can be predicted from the CCIR or USRI model, while the NeQuick analogously uses the CCIR model to achieve the two parameters. Moreover, the NeQuick model is the default description for the topside profile of IRI-2007 and IRI-2012 (Coïsson et al., 2006).

The B-spline approach has advantages in dealing with the non-uniform data and regional modeling due to the endpoint-interpolating and localizing characteristics (Schmidt et al., 2011), which is an effective method to model the ionospheric parameters. For instances, after retrieving the reference component from IRI, Schmidt (2007) calculated the correction term of VTEC as 3-D series expansions in terms of localized B-spline functions. To obtain a 4-D ionospheric model, an F2-layer Chapman function combined with a plasmasphere layer function is employed to describe the vertical electron density distribution, and 3-D NmF2 and hmF2 are modeled through B-spline series expansions based on a combination of ground- and space-based GPS data. NmF2, hmF2 and the scale height HF2 are modeled by applying the endpoint-interpolating polynomial B-splines based on a modified α-chapman function in the description of the vertical electron density distribution (Limberger et al., 2013; Liang et al., 2015).

The two key F2-peak parameters can also be derived from the measurements of global ionosondes and incoherent scatter radars (ISR). However, the distribution of the observation stations is fairly sparse and inhomogeneous due to the expensive cost and big-time-interval observations. Many studies have proved that the performance of the F2 peak parameters in the IRI model has large uncertainties (Zhang et al., 2007). So numerous approaches (Fox and McNamara, 1988; Rejfek et al., 2014) have been advanced to improve the two F2 peak parameters by taking advantages of various modern geodetic measurements, especially the ground-based GNSS observations. In this paper, a two-step algorithm is used to implement 3-D ionospheric imaging with updated background information. Firstly, in order to achieve a precise background for CIT, 2-D *foF2 and M(3000)F2* with respect to the longitude and latitude are modeled by the tensor products of B-spline functions from the ground-based GNSS TEC. The newest verision NeQuick 2 model, rather than the rough modified α-chapman function or IRI-2012, is applied to describe the vertical electron density distribution. Then, the modeled F2 parameters are taken into IRI-2012 to obtain a near real-time 3-D ionospheric distribution. Secondly, the updated IRI-2012 is input as the background ionospheric model and the MART is implemented to retrieve the reconstructed results iteratively. The detail of

the algorithm is presented in Section 2 as well as the data. In Section 3, the results from the new methods are evaluated by the simulation and ground-based GNSS and GNSS Radio Occultation observations as well as ionosonde measurements. Finally, the conclusions are given in Section 4.

2. Improved two-step algorithm

2.1. Updating foF2 and M3000F2

The most-frequently-used ionospheric products are F2 peak parameters from the ionosondes or GNSS RO observations. In addition, TEC is defined as the integral of the electron density along the signal path. Obviously, to obtain the F2 peak parameters using the observations, the electron density should be represented as a function associated with the two F2 peak parameters *foF2 and M(3000)F2*. In earlier studies such as Fonda et al. (2005) and Jakowski (2005), the ionospheric vertical profile is often represented by the combination of a α-chapman function using F2 layer parameters and an exponential decaying function for describing the plasmasphere. The description only takes the F2 layer and the topside of the ionosphere into account. To produce the electron density at a given height, the NeQuick 2 involves five semi-Epstein layers with E, F1 and F2 layer parameters for the bottomside and one semi-Epstein layer involving F2 layer parameters for the topside. The semi-Epstein layer can be expressed as follows:

$$N_{Es}(h;hm;\ m;B) = \frac{4Nm}{\left(1+\exp(\frac{h-hm}{B})\right)^2}\exp\left(\frac{h-hm}{B}\right) \tag{1}$$

where h is the height of the ionosphere, hm and Nm represent the layer peak height and peak electron density, respectively, and B is the layer thickness parameter. These parameters can be empirically obtained or modeled. A key point here is that the peak parameters of the E and F1 layer and most thickness parameters have a tight correlation with *foF2* and *M(3000)F2*. The specific formulas for the bottomside and the topside descriptions can be found in Nava et al. (2008). The two F2 peak parameters and the electron density are determined through the input of time (year, month and universal time), geographic location, height and 12-month-running-mean of 10.7 cm solar radio flux. Here *foF2* and *M(3000)F2* rather than NmF2 and hmF2 are used and other NeQuick parameters are defaulted.

The localizing B-spline approach is used to model the spatial variation of two key parameters. The parameters $\kappa(\lambda,\varphi;t) \in \{foF2,\ M3000F2\}$ are specified at a given time t as the series expansions with respect to the geographical longitude λ and the geographical latitude φ as

$$\kappa(t;\lambda,\varphi) = \sum_{k_1=1}^{K_{J_1}}\sum_{k_2=1}^{K_{J_2}} d_{k_1,k_2}^{J_1,J_2}(t)\phi_{k_1,k_2}^{J_1,J_2}(\lambda,\varphi) \tag{2}$$

where $d_{k_1,k_2}^{J_1,J_2}(t)$ are the unknown time-dependent series coefficients. Here, the 2-D base function $\phi_{k_1,k_2}^{J_1,J_2}(\lambda,\varphi)$ is the tensor product of 1-D B-spline base functions

$$\phi_{k_1,k_2}^{J_1,J_2}(\lambda,\varphi) = \phi_{k_1}^{J_1}(\lambda)\phi_{k_2}^{J_2}(\varphi) \tag{3}$$

We adopt the normalized quadratic B-spline functions as the 1-D base functions with the resolution level $J \in \{J_1, J_2\}$ corresponding to the variable $\{\lambda,\varphi\}$, and the shift $k_i \in \{1,2,\cdots,K_{J_i}\}$ and $i \in \{1,2\}$. $K_J = 2^J + 2$ are the total number of the functions in a 1-D B-spline series. Fig. 1 (a) illustrates the normalized 1-D performance of the quadratic B-spline series in the unit interval [0, 1]. The distance of the adjacent splines is equal to $\Delta = \frac{1}{2^J}$, called the subinterval. Any point has its influence area within 3 splines on which the value of the point is non-zero. For the 2-D B-spline series as shown in Fig. 1(b), the number of the affected splines turn to nine. For a specific location in the 2-D region, i.e., $[\lambda_{\min},\lambda_{\max}] \times [\varphi_{\min},\varphi_{\max}]$, the transformation equations are given by

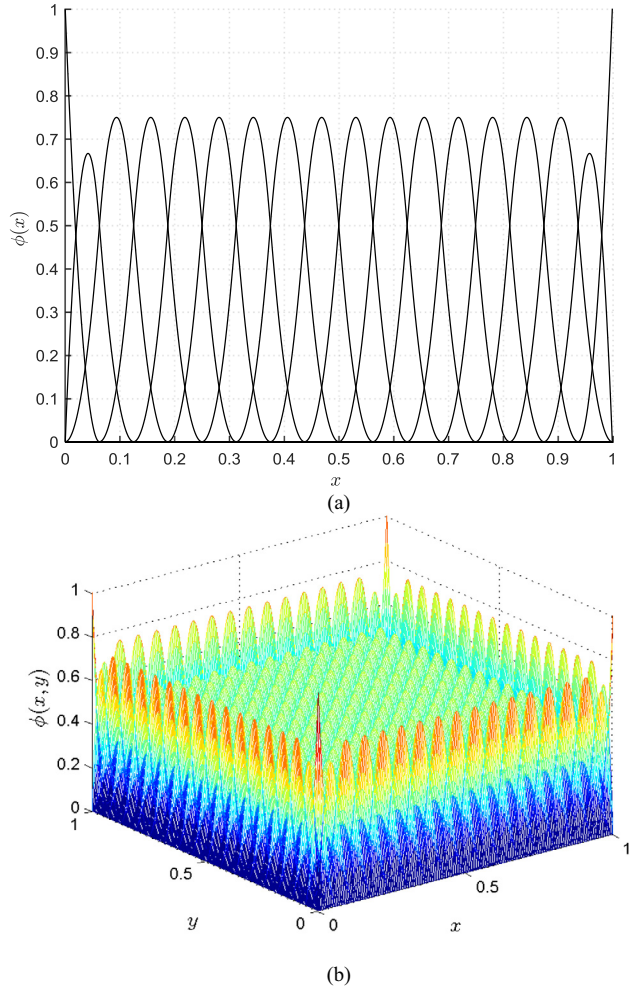

Fig. 1. (a) 1-D series in terms of normalized quadratic B splines at the unit interval [0, 1], (b) 2-D series of tensor product in terms of normalized quadratic B splines with $J = 4$ at the unit area $[0,\ 1] \times [0,\ 1]$.

$$x = \frac{x' - x'_{\min}}{x'_{\max} - x'_{\min}} \text{ with } x' \in (\lambda, \varphi) \tag{4}$$

We establish a Gauss–Markov model with stochastic part to derive the series coefficients of each parameter from a certain observation group

$$l + e_y = \mathbf{A}\Delta d \text{ with } \mathbf{D}(y) = \sigma_y^2 \mathbf{P}_y^{-1} \tag{5}$$

and

$$l = y - y_0 \quad \Delta d = d - d_o \tag{6}$$

Here, the $k \times 1$ vector d contains k unknown series coefficients of $foF2$ or $M(3000)F2$, Δd is the correction from the initial series coefficients d_0. The $n \times k$ matrix A is the design matrix, where n indicates the total number of observations, e_y is the observation noise, l is the difference between the observations y and the approximate values y_0 corresponding to d_0, and $D(y)$ is the $n \times n$ covariance matrix of the observations, where σ_y^2 and $\mathbf{P}_y$ indicate the variance and the weight matrix of the observations, respectively.

In the case of the electron density, the vertical profile function in NeQuick 2 is employed to achieve the representation of the parameters. Due to the highly nonlinear in each parameter, we implement the linearization to get the linear expression of any electron density Ne_i with the parameter $\kappa \in \{foF2, M3000F2\}$ and thus yield

$$Ne_i = \left(\frac{\partial Ne_i^0}{\partial \kappa} \cdot \frac{\partial \kappa}{\partial d}\right)\Big|_0 \Delta d + Ne_i^0 + e_{Ne_i^0} \tag{7}$$

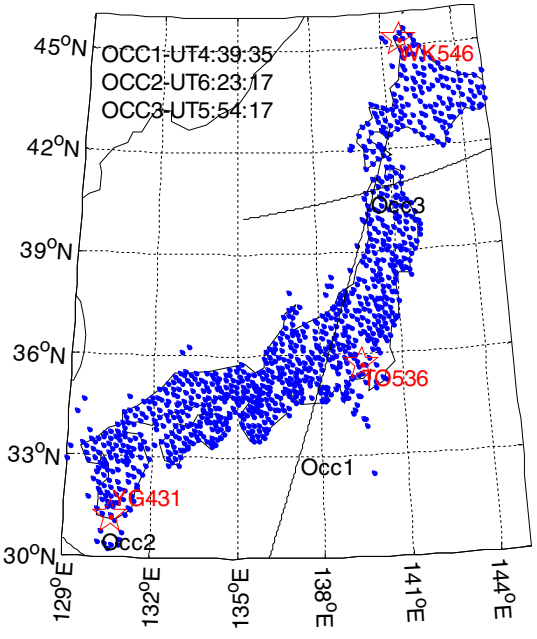

Fig. 2. The distribution of GNSS stations (blue pentagrams) from GEONET and IGS, the moving track of the occultation tangents (black line) from the COSMIC GPS Radio Occultation and three ionosondes (red pentagrams) in the reconstructed region. (For interpretation of the references to color in this figure legend, the reader is referred to the web version of this article.)

where $e_{Ne_i^0}$ is the error from the observations and Ne_i^0 indicates the linear approximation by using the initial coefficients d_0. Based on the Eq. (7), additional numerical integration is performed using the TEC from ground-based GNSS observations. We adopt the similar effective integration strategy as the NeQuick2 does. The ionosphere is divided into NL layers, and each layer includes NST steps with respect to the layer $\boldsymbol{i}$. For every step, Gauss–Legendre integration is implemented with NG_i nodes. Afterwards, TEC can be expressed as the numerical integration by

$$TEC_j + e_{TEC_j} = \sum_{j=1}^{L} \Delta s_j Ne_j^0 \text{ with } L = \sum_{i=1}^{NL} NG_i * NST_i \tag{8}$$

where e_{TEC_j} is the error mainly caused by the numerical discretization, Δs_j is the length of the jth step, and L indicates the total number of steps.

The priori information of the series coefficients is introduced to balance the data gaps due to the inhomogenious and sparse data distributions. The priori value cannot influence the area far away from the data. The priori information can be regarded as another observation group, called pseudo-observation group, and is introduced with the variance σ_μ^2 and the covariance matrix $\mathbf{D}(\mu)$ as follows

$$\mu_d + e_\mu = d \text{ with } \mathbf{D}(\mu) = \sigma_\mu^2 \mathbf{P}_\mu^{-1} \tag{9}$$

where $\mathbf{P}_\mu$ is the $k \times k$ weight matrix. Therefore, the series coefficients are estimated based on the combination of various observation techniques especially including the pseudo-observations of the priori coefficients. Assumed that these techniques are independent of each other, we infer the normal equation as follows

$$\left(\sum_{i=1}^{O} \frac{1}{\sigma_i^2} \mathbf{A}_i^T \mathbf{P}_i \mathbf{A}_i + \frac{1}{\sigma_\mu^2} \mathbf{P}_\mu\right) \Delta d = \sum_{i=1}^{O} \frac{1}{\sigma_i^2} \mathbf{A}_i^T \mathbf{P}_i (y_i - y_i^0) + \frac{1}{\sigma_\mu^2} \mathbf{P}_\mu (\mu_d - d_0) \tag{10}$$

where the subscript i indicates the i^{th} real observation technique. Ground-based GNSS observations are used to inverse the parameters and the unit matrix is chosen as the weight matrix. Moreover, the priori information and the initial series coefficients can be derived from the same parameter model while the precision of the initial vector is subject to the resolution of the B spline series. In our study, the CCIR model used in NeQuick 2 (or IRI) is considered to provide both, and the weight matrix is identified as a positive definited weight matrix. To determine the unknown variances, variance component estimation (VCE) is performed by the stochastic trace estimator. The detailed description is given by Koch and Kusche (2002). Involving the above normal equation and VCE technique, we estimate and improve $foF2$ and $M(3000)F2$ through an iterative procedure. $foF2$ and $M(3000)F2$ are estimated separately, which may stabilize the model and will avoid the discussion of the correlation between $foF2$ and $M(3000)F2$.

Table 1
Statistical results of the mean relative deviations of the parameters from IRI-2012 model.

Maximum deviation /*foF2*, Maximum deviation /*M(3000)F2*	Average Deviation before updation		Average Deviation after updation by B-splines	
	foF2	*M(3000)F2*	*foF2*	*M(3000)F2*
20%/*foF2*, 10% /*M(3000)F2*	13.7%	6.85%	8.23%	5.81%
30%/*foF2*, 15% /*M(3000)F2*	15.3%	7.90%	9.01%	6.21%

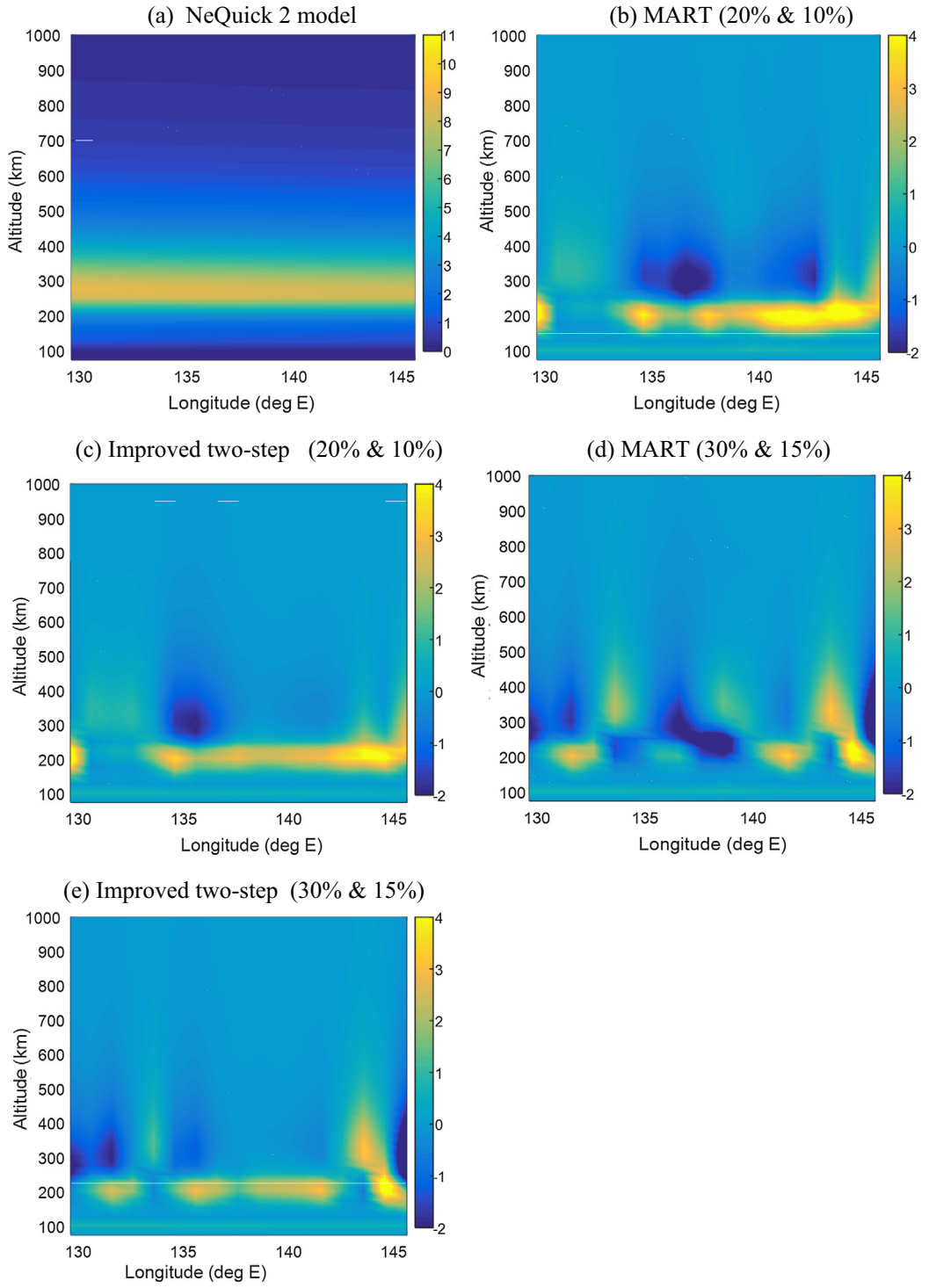

Fig. 3. IED distributions at 38° N with different methods. (a) NeQuick 2 model. (b) and (c) reconstructed results by MART and the improved two-step algorithms at *foF2* parameters with the maximal relative deviation: *foF2* parameters within 20%, M3000F2 parameters within 10%. (d) and (e) reconstructed results by MART and the improved two-step algorithms at *foF2* parameters with the maximal relative deviation: *foF2* parameters within 30%, M3000F2 parameters within 15%.

2.2. An improved two-step algorithm

At the first step, based on the NeQuick2 model, we estimate the parameters of *foF2* and *M(3000)F2* using the B-spline methods from real observations. Here the order J is selected according to the resolution of observations. Then, the improved *foF2* and *M(3000)F2* are taken as the input to make the IRI-2012 closer to the real ionosphere while NeQuick 2 can be also improved by absorbing the updated *foF2* and *M(3000)F2*.

Afterwards, the background ionosphere is derived from the updated IRI-2012, and the MART algorithm is implemented based on the pixel-based model

$$\mathbf{y}_{n\times 1} = \mathbf{A}_{n\times p}\mathbf{x}_{p\times 1} + \varepsilon_{n\times 1} \tag{11}$$

$$x_j^{(m+1)} = x_j^{(m)}\left(\frac{y_i}{\langle A_i, x^{(k)}\rangle}\right)^{\gamma_k A_{ij}/|A_i|} \tag{12}$$

where $\mathbf{y}_{n\times 1}$ consists of m TEC measurements and y_i is the i^{th} component of $\mathbf{y}_{n\times 1}$, x_j indicates the j^{th} member in the vector $\mathbf{x}_{p\times 1}$ composed of p unknown electron density in all voxels, and m indicates the m^{th} iteration. $\mathbf{A}_{n\times p}$ is the design matrix containing all the intercept of the ray path traversing the grids and A_i is the vector corresponding to the i^{th} row of $\mathbf{A}_{n\times p}$. $|A_i|$ is the total length of the i^{th} ray path. $\varepsilon_{n\times 1}$ includes the observation noise and discretization error. γ_k is the relaxation parameter and lies in between 0 and 1.

According to the formula of the MART algorithm, each ray path of TEC measurements updates the electron density of the voxels, in which the ray path passes through. Therefore, the influence area of each ray path is composed of the pixel points along the ray path while that, as for B-spline methods, becomes the vertical space extended from the total horizontal coverage of nine 2-D B-splines corresponding to each point of the ray path. Combination of the B-spline methods and the MART algorithm, the new two-step approach has improved CIT estimation with the endpoint-interpolating and localizing characteristics. The application of the local smoothness from B splines and NeQuick 2 model avoids unreasonable gradient in regional electron density distribution, but it is still not real ionospheric structure.

3. Results and discussion

3.1. 3-D ionospheric image from GNSS

About 900 GPS stations from GEONET are used in Japan from 30° to 46° in latitude, 129° to 145° in longitude and 75 km to 2000 km in height (Fig. 2). To obtain high-precision GNSS TEC, the dual-frequency pseudo-ranges smoothed by carrier phases are used and the differential code biases (DCBs) of GNSS satellite and receiver are estimated (Jin et al. 2012, 2016). The resolution of the GNSS receiver stations can reach as high as 0.25°x0.25°, so we set the order J as 4 to get a high resolution of the parameters using the B-spline model, resulting in $18*18*2 = 324$ unknown series coefficients. The pixel intervals are 1°, 1° and 25 km in latitude, longitude and height, respectively. Instantaneous IED images are obtained by the MART and two-step method from GNSS observations within a 3-min period, which will provide about ten thousands of appropriate GNSS signal rays for CIT reconstruction. Actually, the utilization of 3-min observations is not for achieving more GNSS signal rays, but mainly aims at increasing the weight of the real observations in the coefficient evaluation of *foF2* and *M(3000)F2*. The ionospheric validation data scaled from ionosondes in Japan can be obtained from the World Data Center (WDC) for Ionosphere and Space Weather operated by the National Institute of Information and Communications Technology (NICT), and National Geophysical Data Center (NGDC) using Expert System for Ionogram Reduction (ESIR) (Eccles et al., 2011).

3.2. Validation from simulation results

To demonstrate the feasibility and superiority of the new approach, we carried out the experiment with simulated data. To drive the simulation experiment more credible, the real GNSS rays are adopted and deviations are imposed on the original *foF2* and *M(3000)F2*. Detailed process descriptions are given as follows:

(1) The simulated GNSS TEC is derived by providing real locations of GNSS receivers and satellites to the NeQuick software with time and a 12-month

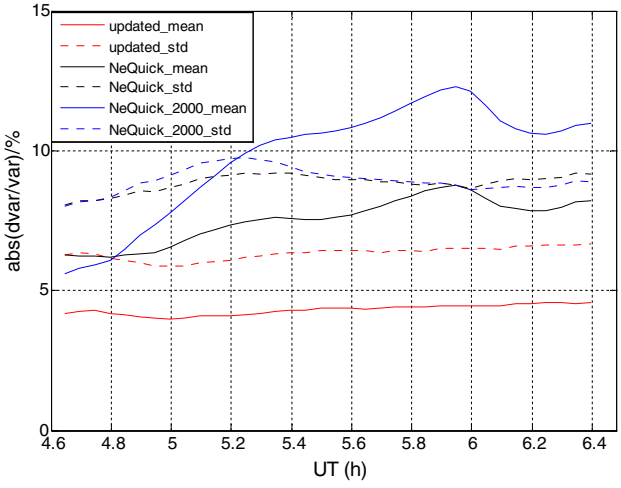

Fig. 4. The averages (solid line) and the standard deviations (dotted line) of the relative TEC residuals obtained from the NeQuick 2 model within the range from the GNSS receivers to the GPS satellites along the ray path (black line), the NeQuick 2 model within the range from 75 km to 2000 km along the ray path (blue line), and the updated NeQuick 2 model (red line). (For interpretation of the references to color in this figure legend, the reader is referred to the web version of this article.)

running average of 10.7 cm solar radio flux. In addition, 5% of the random noise is added to the simulated TEC.

(2) We inverse the series coefficients of the parameters from CCIR in either NeQuick 2 or IRI-2012. The 20% and 30% maximum deviations are added to the original series coefficients of *foF2* as the prior series coefficients called $foF2_{dev}$, respectively. Here the subscript *dev* indicates the deviated level. For *M (3000)F2*, the deviations of the series coefficients are within 10% and 15% respectively, resulting in $M(3000)F2_{dev}$. The initial series coefficients are obtained at the same time.

(3) Modeling the series coefficients of the two key parameters, which yield $foF2^{up}_{dev}$ and $M(3000)F2^{up}_{dev}$.

(4) We input the deviated parameters and the updated deviated parameters into the IRI-2012 model to gain the ionospheric background for the MART, respectively.

(5) We reconstruct the ionospheric images using MART algorithm and our improved two-step algorithm, respectively.

The ionospheric vertical profiles are obtained from different methods at different deviation levels at UT 6:00 on March 11, 2011. The comparisons show that the electron density profiles reconstructed from our method are in general closer to the profiles from the NeQuick 2 model than those obtained using only MART, which may be attributed to the improvement of the parameters in IRI-2012 by B-spline methods. Table 1 shows the statistical results of the mean relative deviations of the series coefficients that are changed by B-spline methods. The great and slight improvements are reflected in the *foF2* and *M(3000)F2* estimations, respectively. As shown in Fig. 3, compared with the profiles from the deviated IRI-2012 without an updation, the profiles from the deviated IRI-2012 with updation agree better with the NeQuick profiles. Furthermore,

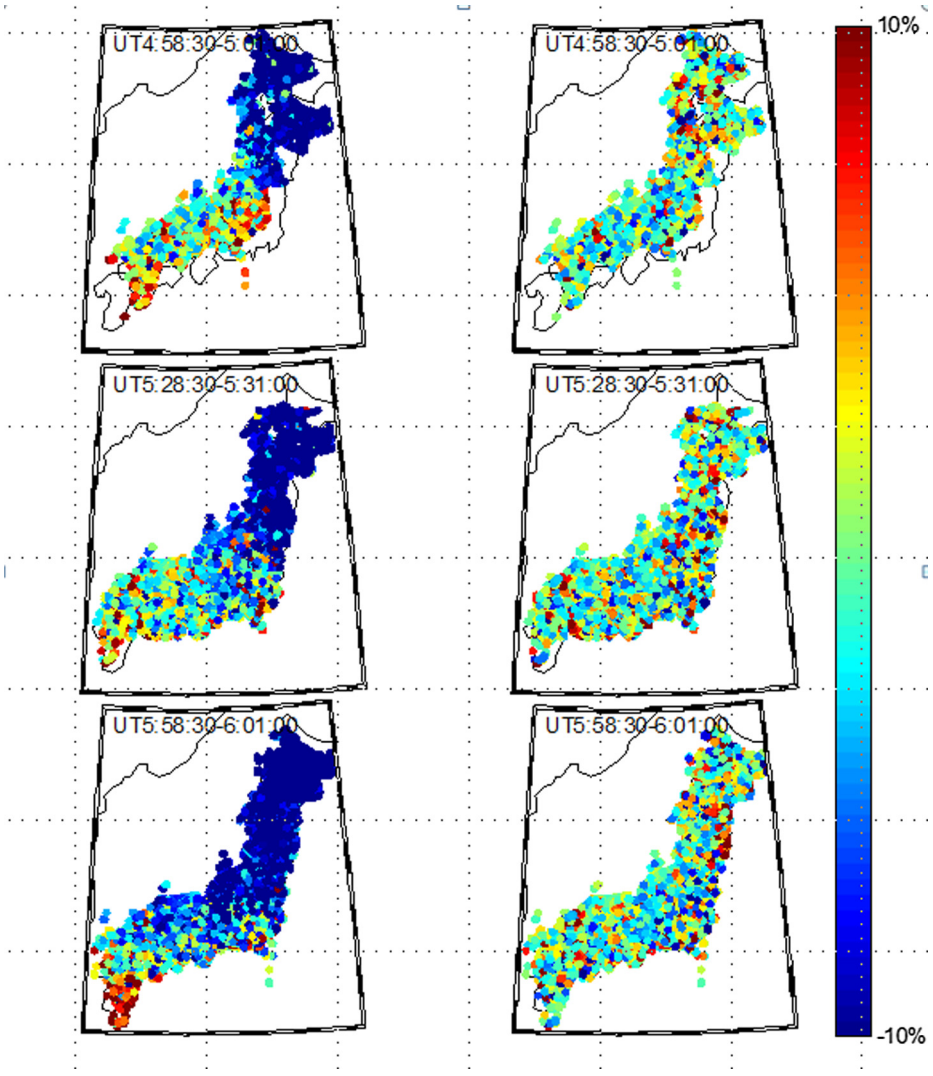

Fig. 5. The distributions of the relative TEC residuals at the pierce point obtained from NeQuick 2 model (left) and the updated NeQuick 2 mode (right) at different time.

the number of iterations before converges are 20 and 15 in MART reconstruction and in the reconstruction of the new method, respectively. The results demonstrate that the improved two-step algorithm has the superiority and higher computational efficiency than the MART algorithm.

As shown in Fig. 3, we use two methods to achieve IED distribution difference from the NeQuick model at different deviation levels. The electron density diversity obtained by the two methods is the same in the areas where observations are not available, and this difference is caused by the simulated systematic deviations imposed on IRI-2012 model. In the data-coverage area, the reconstructed images from the two-step algorithm show a smaller discrepancy with the images derived from the NeQuick model than those from MART. Moreover, in the profiles from the two-step algorithm, the consistency with the NeQuick model is also found at the edge of the data-available area, as the utilization of B-spline methods extends the correction zones. Hence, the comparison further validates that our two-step is more appropriate to obtain high-quality tomographic images.

3.3. Evaluation by observations

We further use real measurements to validate the improved two-step algorithm. 3-min time series of 3-D IED distributions are obtained from ground-based GNSS observations on March 11, 2011. For comparison between different algorithms, the original IRI-2012 input as the background of MART algorithm should employ CCIR model rather than USRI model, while inputting the parameters from CCIR of NeQuick into IRI-2012 is an appropriate and better way to avoid the slight discrepancy of CCIR model in IRI-2012 and NeQuick 2.

The updated F2 parameters have a direct impact on the performance of the new method. Hence, the first step

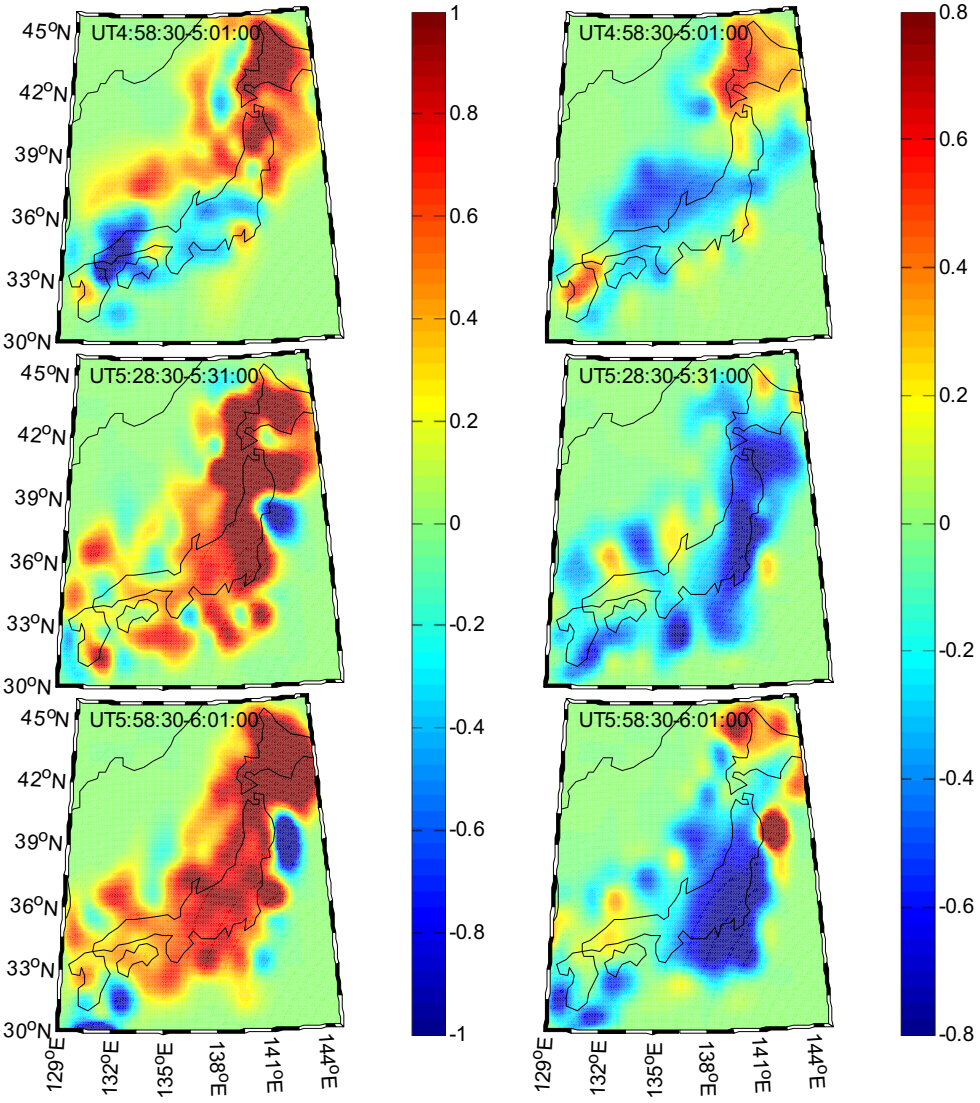

Fig. 6. The distributions of the difference between the updated *foF2* by the B-spline method and the *foF2* from the NeQuick model (left), and the distributions of the difference between the updated M3000F2 by the B-spline method and the M3000F2 from the NeQuick model (right).

towards performs the assessment of *foF2* and *M(3000)F2* modeled by B-spline approaches. Moreover, how the updated parameters influence the ionospheric corrections using the NeQuick model also should pay attention. Compared with NeQuick model, it costs ten times or more to derive TEC values or IED distributions by using the IRI-2012 model, which can be attributed to particular design for rapid calculation in the NeQuick model. Thus, we estimate *foF2* and *M(3000)F2* involving the updated NeQuick model rather than the updated IRI-2012 model, and the performance of ionospheric corrections are assessed together.

Fig. 4 shows the averages and standard deviations of the relative TEC residuals using different approaches. The averages and standard deviations using the B-spline modeling approach are below 5% and around 7%, respectively, both of which are more than 20% and less than the averages and standard deviations derived from the original NeQuick model within reconstructed ranges or receiver-satellite range. Fig. 5 shows the distributions of the relative TEC residuals from different methods. The shade of color varies with the values of the relative TEC residuals, which are limited to 10% maximum. The negative big residuals from the original NeQuick 2 spread throughout the high-latitude area with data coverage and turn to be positive towards the low-latitude area, which is due to the system bias from the original NeQuick 2. In contrast, the residuals from the updated NeQuick model are smaller with uniform distributions. Fig. 6 shows the parameter corrections in the areas where data are available, and the CCIR model may underestimate *foF2* and overestimates *M(3000)F2* in most areas. Therefore, the results demonstrate the B-spline modeling method has advantages to estimate the ionospheric parameters and improve the ionospheric corrections.

As shown in Fig. 7, the improved F2 parameters at a given time are input into the NeQuick model to predict the effects of ionospheric corrections. The averages and standard deviations of the relative TEC residuals using the updated F2 parameters are smaller than those from the original NeQuick model within 15 min. It means that the updated NeQuick model driven by the improved *foF2* and *M(3000)F2* is a better predictor for ionospheric errors in a certain time, whose time, of course, is correlated well with the condition of the ionosphere. Besides, only less than 35% of the series coefficients is changed by more than 5% due to the sparse data distribution, which is propitious to release the improved parameters for single-frequency ionospheric correction.

Fig. 8 shows the independent comparisons of vertical IED profiles from different methods. As for the validation data, the electron density profiles obtained by ESIR are identified by the ionosonde parameters from WDC of NICT. With closer background profiles, the profiles from

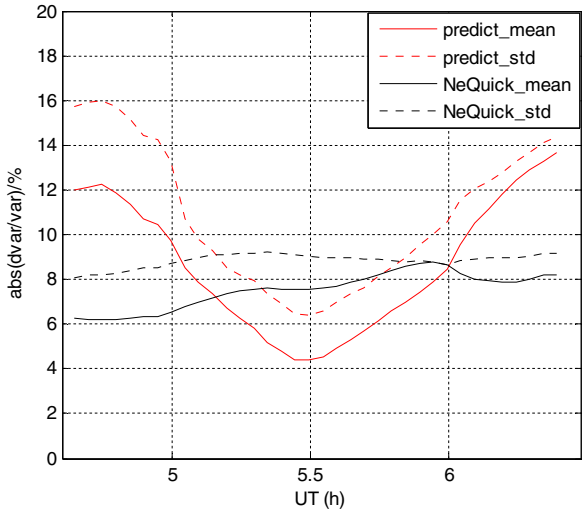

Fig. 7. Comparison of the averages (solid line) and the standard deviations (dotted line) of the TEC residual derived from the original NeQuick model within the range from the GNSS receivers to the GPS satellites along the ray path (black line), and the predicted NeQuick model (red line) obtained by inputting the improved *foF2* and *M(3000)F2* modeled at a given time of UT 5:30. (For interpretation of the references to color in this figure legend, the reader is referred to the web version of this article.)

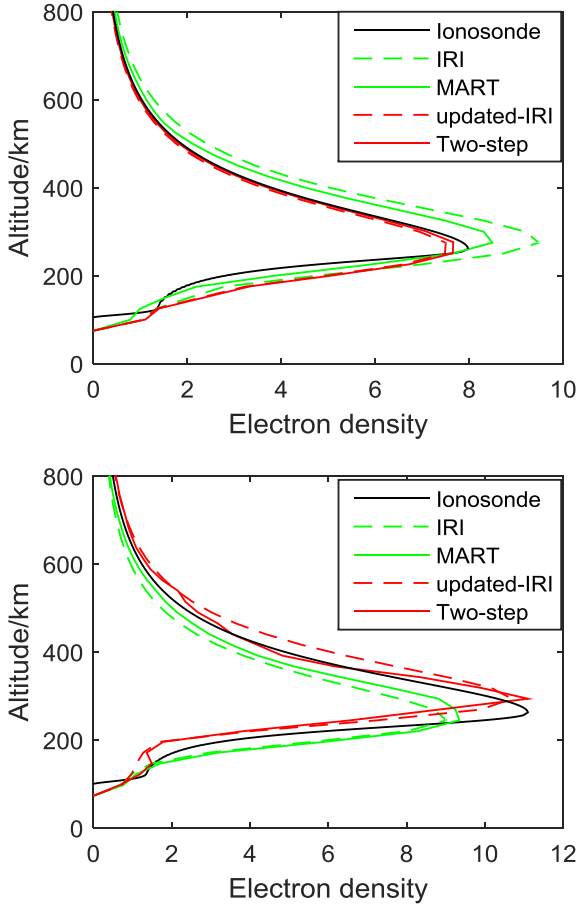

Fig. 8. Electron density profiles reconstructed from ionosonde measurements (black solid line), IRI-2012 model (green dotted line), MART (blue solid line), the updated IRI-2012 model (red dotted line), and the two-step algorithm (red solid line) at the ionosonde of Yamagawa (31.2° N, 130.62° E) at UT 2:00 (left) and UT 6:30 (right) on March 11, 2011. (For interpretation of the references to color in this figure legend, the reader is referred to the web version of this article.)

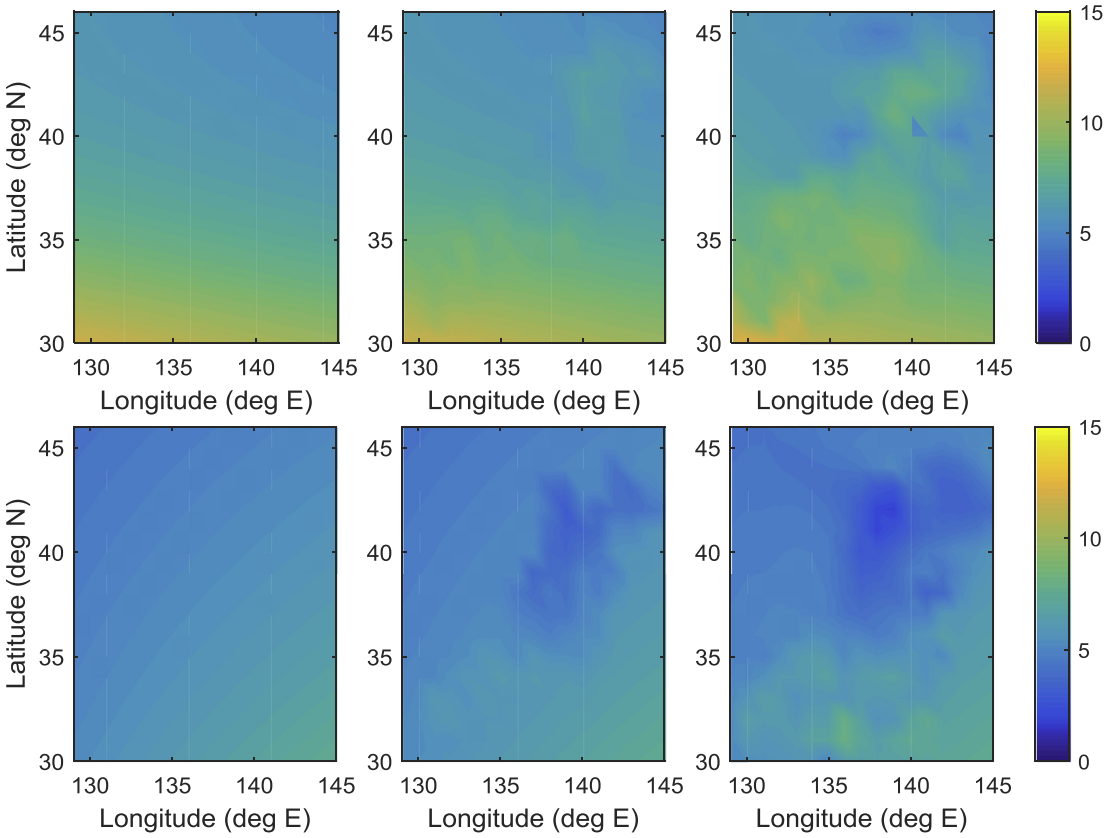

Fig. 9. IED profiles obtained from IRI-2012 (left), MART (middle), the improved two-step algorithm (right) at 300 km height at UT6:00 (first line) and UT 23:00 (second line) on March 11, 2011. The unit of the color bar is 10^{11} el/m^3.

our method show higher consistency with ionosonde data. This result confirms the advantages of the new algorithm in 3-D ionospheric imaging. As seen in Fig. 9, the IED distributions change with respect to the time, longitude and latitude, and are in good agreement with the real variation regulation of the ionosphere. The localization feature possessed by the new method is clearly displayed, and the size of the local detail is associated with the order J, which extends the correction areas meanwhile. Therefore, the capability of the two-step algorithm is further validated.

Further, we further use above methods to analyze GPS observations and obtain vertical IED profiles on other days with low solar activity of F10.7 cm and with high solar activity of F10.7 cm, and conclusions are almost similar, but with large differences during high solar actitivities due to imprecise empicical models. Our improved two-step iterative algorithm will improve 3-D ionospheric tomography from dense GNSS observations. However, the low accuracy is mainly due to low accuracy of empirical models, e.g., NeQuick-2 and IRI-2012. In the future, it needs to further improve the empirical model (e.g., IRI-2016 and NeQuick-2).

4. Conclusions

An improved two-step algorithm is developed using the MART with combined B-spline modeling methods. At the first step of the new algorithm, the NeQuick 2 model is employed to provide the vertical ionospheric structure, and then B-spline modeling methods are used to improve the 2-D F2 key parameters *foF2* and *M(3000)F2* with respect to the longitude and latitude. Simulation results and real GNSS observations verify the reliability and superiority of the new algorithm. The results in terms of TEC residuals show the ability of B-spline modeling methods to improve the F2 key parameters. Actually, the localizing characteristics of the B-spline methods, combined with MART, prompt the new algorithm a local method. The comparisons with ionosonde measurements further validate the advantages of our new method. Since the NeQuick is designed particularly for trans-ionospheric propagation applications, the performance of the updated NeQuick 2 also decreases more than 20% ionospheric errors in the original NeQuick model and has a uniform distribution of TEC residuals. With few coefficients changed over 5%, the modeled series coefficient is fitting to be released for single-frequency ionospheric correction. The B-spline methods amount to low-pass filtering, and multi-level estimations with different J can easily provide the IED within a given frequency band. Furthermore, the B-spline model can be easily extended to 3-D and 4-D model. In the future, a 4-D ionospheric model will be extended with taking advantages of various modern geodetic measurements, especially GNSS RO data.

Acknowledgments

The authors would thank Takuya Tsugawa from Space Environment Laboratory at NICT in Japan for providing 15-min manually scaled ionospheric factor and Yenca Migoya-Orue from Telecommunications/ICT for Development Laboratory at Abdus Salam International Centre for Theoretical Physics for NeQuick 2 routine package. This work was supported by the National Natural Science Foundation of China (NSFC) Project (Grant Nos. 11573052 and 41761134092).

References

Aa, E., Liu, S., Huang, W., Shi, L., Gong, J., Chen, Y., Li, J., 2016. Regional 3D ionospheric electron density specification on the basis of data assimilation of ground-based GNSS and radio occultation data. Space Weather 14, 433–448. https://doi.org/10.1002/2016SW001363.

Angrisano, A., Gaglione, S., Gioia, C., Massaro, M., Robustelli, U., 2013. Assessment of NeQuick ionospheric model for Galileo single-frequency users. Acta Geophysica 61 (6), 1457–1476.

Austen, J.R., Franke, S.J., Liu, C.H., Yeh, K.C., 1986. Application of computerized tomography techniques to ionospheric research. In: International Beacon Satellite Symposium on Radio Beacon Contribution to the Study of Ionization and Dynamics of the Ionosphere and to Corrections to Geodesy and Technical Workshop, vol. 1, 25-35.

Bhuyan, K., Singh, S.B., Bhuyan, P.K., 2004. Application of generalized singular value decomposition to ionospheric tomography. Annales Geophysicae 22 (10), 3437–3444.

Bust, G.S., Mitchell, C.N., 2008. History, current state, and future directions of ionospheric imaging. Rev. Geophys. 46(1), RG1003, doi: 10.1029/2006RG000212.

Coïsson, P., Radicella, S.M., Leitinger, R., Nava, B., 2006. Topside electron density in IRI and NeQuick: features and limitations. Adv. Space Res. 37 (5), 937–942.

Eccles, V., Rice, D.D., Sojka, J.J., Valladares, C.E., Bullett, T., Chau, J.L., 2011. Lunar atmospheric tidal effects in the plasma drifts observed by the Low-Latitude Ionospheric Sensor Network. J. Geophys. Res.: Space Phys. 116(A7), 116, A07309, doi: 10.1029/2010JA016282.

Fonda, C., Coïsson, P., Nava, B., Radicella, S.M., 2005. Comparison of analytical functions used to describe topside electron density profiles with satellite data. Ann. Geophys. 48 (3), 491–495. https://doi.org/10.4401/ag-3213.

Fox, M.W., McNamara, L.F., 1988. Improved world-wide maps of monthly median foF2. J. Atmosp. Terrestrial Phys. 50 (12), 1077–1086.

Jakowski, N., 2005. Ionospheric GPS radio occultation measurements on board CHAMP. GPS Sol. 9 (2), 88–95.

Jin, R., Jin, S.G., Feng, G., 2012. M_DCB: Matlab code for estimating GNSS satellite and receiver differential code biases. GPS Solutions 16 (4), 541–548.

Jin, S.G., Wang, J., Zhang, H., Zhu, W.Y., 2004. Real-time monitoring and prediction of the total ionospheric electron content by means of GPS observations. Chin. Astron. Astrophys. 28 (3), 331–337. https://doi.org/10.1016/j.chinastron.2004.07.008.

Jin, S.G., Park, P.H., 2006. Strain accumulation in South Korea inferred from GPS measurements. Earth Planets Space 58 (5), 529–534. https://doi.org/10.1186/BF03351950.

Jin, S.G., Park, J.U., Wang, J.L., Choi, B.K., Park, P.H., 2006. Electron density profiles derived from ground-based GPS observations. J. Navigation 59 (03), 395–401.

Jin, S.G., Park, J.U., 2007. GPS ionospheric tomography: a comparison with the IRI-2001 model over South Korea. Earth, Planets and Space 59 (4), 287–292.

Jin, S.G., Cho, J., Park, J., 2007. Ionospheric slab thickness and its seasonal variations observed by GPS. J. Atmos. Sol.-Terr. Phys. 69 (15), 1864–1870. https://doi.org/10.1016/j.jastp.2007.07.008.

Jin, S.G., Luo, O., Park, P., 2008. GPS observations of the ionospheric F2-layer behavior during the 20th November 2003 geomagnetic storm over South Korea. J. Geodesy 82 (12), 883–892. https://doi.org/10.1007/s00190-008-0217-x.

Jin, S.G., Feng, G.P., Gleason, S., 2011. Remote sensing using GNSS signals: current status and future directions. Adv. Space Res. 47 (10), 1645–1653.

Jin, S.G, Cardellach, E., Xie, F., 2013. GNSS Remote Sensing: Theory, Methods and Applications. Springer, Germany, p. 276.

Jin, S.G., Jin, R., Li, D., 2016. Assessment of BeiDou differential code bias variations from multi-GNSS network observations. Ann. Geophs. 34 (2), 259–269. https://doi.org/10.5194/angeo-34-259-2016.

Koch, K.R., Kusche, J., 2002. Regularization of geopotential determination from satellite data by variance components. J. Geodesy 76 (5), 259–268.

Kunitake, M., Ohtaka, K., Maruyama, T., Tokumaru, M., Morioka, A., Watanabe, S., 1995. Tomographic imaging of the ionosphere over Japan by the modified truncated SVD method. Annales Geophysicae 13 (12), 1303–1310.

Kunitsyn, V.E., Nesterov, I.A., Padokhin, A.M., Tumanova, Y.S., 2011. Ionospheric radio tomography based on the GPS/GLONASS navigation systems. J. Commun. Technol. Electron. 56 (11), 1269–1281.

Liang, W., Limberger, M., Schmidt, M., Dettmering, D., Hugentobler, U., Bilitza, D., Gerzen, T., 2015. Regional modeling of ionospheric peak parameters using GNSS data—an update for IRI. Adv. Space Res. 55 (8), 1981–1993.

Limberger, M., Liang, W., Schmidt, M., Dettmering, D., Hugentobler, U., 2013. Regional representation of F2 Chapman parameters based on electron density profiles. Annales Geophysicae 31 (12), 2215–2227.

Montenbruck, O., Hauschild, A., Steigenberger, P., 2014. Differential code bias estimation using multi-GNSS observations and global ionosphere maps. Navigation 61 (3), 191–201.

Najibi, N., Jin, S.G., 2013. Physical reflectivity and polarization characteristics for snow and ice-covered surfaces interacting with GPS signals. Remote Sens. 5 (8), 4006–4030. https://doi.org/10.3390/rs5084006.

Nava, B., Coisson, P., Radicella, S.M., 2008. A new version of the NeQuick ionosphere electron density model. J. Atmos. Solar-Terrestrial Phys. 70 (15), 1856–1862.

Razin, M.R.G., 2016. Development and analysis of 3D ionosphere modeling using base functions and GPS data over Iran. Acta Geodaetica et Geophysica 51 (1), 95–111.

Rejfek, L., Kouba, D., Mosna, Z., 2014. Measurement of critical frequency of the layer F2 by the using of the GPS. In: Radioelektronika (RADIOELEKTRONIKA), 2014 24th International Conference IEEE, p.1–4.

Schmidt, M., Dettmering, D., Mößmer, M., Wang, Y., Zhang, J., 2011. Comparison of spherical harmonic and B spline models for the vertical total electron content. Radio Sci. 46 (6), 1–8.

Schmidt, M., 2007. Wavelet modelling in support of IRI. Adv. Space Res. 39 (5), 932–940.

Seemala, G.K., Yamamoto, M., Saito, A., Chen, C.H., 2014. Three-dimensional GPS ionospheric tomography over Japan using constrained least squares. J. Geophys. Res.: Space Phys. 119 (4), 3044–3052.

Wen, D., Yuan, Y., Ou, J., Huo, X., Zhang, K., 2007. Three-dimensional ionospheric tomography by an improved algebraic reconstruction technique. GPS Sol. 11 (4), 251–258.

Yao, Y., Kong, J., Tang, J., 2015. A new ionosphere tomography algorithm with two-grid virtual observations constraints and three-dimensional velocity profile. IEEE Trans. Geosci. Remote Sens. 53 (5), 2373–2383.

Yu, X., She, C., Zhen, W., Bruno, N., Liu, D., Yue, X., Xu, J., 2015. Ionospheric correction based on ingestion of global ionospheric maps

into the NeQuick 2 model. Sci. World J. 3–4, 376702. https://doi.org/10.1155/2015/376702.

Yue, X., Schreiner, W.S., Kuo, Y.H., Hunt, D.C., Wang, W., Solomon, S. C., Wickert, J., 2012. Global 3-D ionospheric electron density reanalysis based on multisource data assimilation. J. Geophys. Res.: Space Phys. 117 (A9), 667–672.

Zhang, M.L., Shi, J.K., Wang, X., Shang, S.P., Wu, S.Z., 2007. Ionospheric behavior of the F2 peak parameters foF2 and hmF2 at Hainan and comparisons with IRI model predictions. Adv. Space Res. 39 (5), 661–667.